May 2017

Beyond 3 AU from the Sun: The Hypervolatiles CH4, C2H6, and CO in the Distant Comet C/2006 W3 (Christensen)

Boncho Bonev
American University

Geronimo Villanueva
Goddard Space Flight Center

Michael DiSanti
Goddard Space Flight Center

Hermann Boehnhardt
Max Planck Society

Manuela Lippi
Max Planck Society

See next page for additional authors

Recommended Citation

Bonev, Boncho; Villanueva, Geronimo; DiSanti, Michael; Boehnhardt, Hermann; Lippi, Manuela; Gibb, Erika; Paganini, Lucas; and Mumma, Michael, "Beyond 3 AU from the Sun: The Hypervolatiles CH4, C2H6, and CO in the Distant Comet C/2006 W3 (Christensen)" (2017). *Physics Faculty Works*. 21.
DOI: https://doi.org/10.3847/1538-3881/aa64dd
Available at: https://irl.umsl.edu/physics-faculty/21

The Astronomical Journal, 153:241 (12pp), 2017 May https://doi.org/10.3847/1538-3881/aa64dd

Beyond 3 au from the Sun: The Hypervolatiles CH_4, C_2H_6, and CO in the Distant Comet C/2006 W3 (Christensen)*

Boncho P. Bonev[1,2,3], Geronimo L. Villanueva[2,3,4], Michael A. DiSanti[2,4], Hermann Boehnhardt[5], Manuela Lippi[5], Erika L. Gibb[2,6], Lucas Paganini[2,3], and Michael J. Mumma[2,4]
[1] Department of Physics, American University, Washington, DC 20016, USA; bonev@american.edu
[2] NASA Goddard Center For Astrobiology, NASA GSFC, Mail Stop 690, Greenbelt, MD 20771, USA
[3] Department of Physics, Catholic University of America, Washington, DC 20061, USA
[4] Solar System Exploration Division, Mail Stop 690, Greenbelt, MD 20771, USA
[5] Max-Planck-Institut für Sonnensystemforschung, Justus-von-Liebig-Weg 3, 37077 Gottingen, Germany
[6] Department of Physics and Astronomy, University of Missouri–St. Louis, St. Louis, MO 63121, USA
Received 2016 May 27; revised 2017 February 28; accepted 2017 March 2; published 2017 May 3

Abstract

Comet C/2006 W3 (Christensen) remained outside a heliocentric distance (R_h) of 3.1 au throughout its apparition, but it presented an exceptional opportunity to directly sense a suite of molecules released from its nucleus. The Cryogenic Infrared Echelle Spectrograph at ESO-VLT detected infrared emissions from the three "hypervolatiles" (CO, CH_4, and C_2H_6) that have the lowest sublimation temperatures among species that are commonly studied in comets by remote sensing. Even at $R_h = 3.25$ au, the production rate of each molecule exceeded those measured for the same species in a number of other comets, although these comets were observed much closer to the Sun. Detections of CO at $R_h = 3.25$, 4.03, and 4.73 au constrained its post-perihelion decrease in production rate, which most likely dominated the outgassing. At 3.25 au, our measured abundances scaled as $CO/CH_4/C_2H_6 \approx 100/4.4/2.1$. The C_2H_6/CH_4 ratio falls within the range of previously studied comets at $R_h < 2$ au, while CO/CH_4 is comparatively high and similar to in situ measurements from *Rosetta* at ~10 km from the nucleus of 67P/Churyumov-Gerasimenko conducted at a very similar R_h (3.15 au). The independent detections of H_2O (*Herschel Space Observatory*) and CO (this work) imply a coma abundance $H_2O/CO \approx 20\%$ in C/2006 W3 near $R_h = 5$ au. All these measurements are of high value for constraining models of nucleus sublimation (plausibly CO-driven) beyond $R_h = 3$ au, where molecular detections in comets are still especially sparse.

Key words: comets: general – comets: individual (C/2006 W3 Christensen) – techniques: spectroscopic

1. Activity of Distant Comets

Comet C/2006 W3 (Christensen) presented the best opportunity since the 1997 apparition of C/1995 O1 Hale-Bopp for detailed spectroscopic remote sensing studies of cometary gaseous activity at heliocentric distances (R_h) larger than 3 au. Such observations far from the Sun are of value for constraining the nucleus structure and for better understanding the sublimation of primary volatiles, that is, those that are originally stored as ices in comet nuclei. While water is the most abundant gas in the atmospheres of comets within ~2–3 au from the Sun, water ice becomes increasingly inactive on more distant comets and more volatile ices (such as CO, CO_2, C_2H_6, CH_4, etc.) must contribute substantially to outgassing from their nuclei.

Analyses of light curves and photometry of the dust coma have provided significant historical evidence for cometary activity at large R_h (Marsden & Roemer 1982; Meech & Svoren 2004; Mazzotta Epifani et al. 2007, 2008, 2009; Meech et al. 2009, 2013; Lamy et al. 2014, and references therein). Direct molecular detections in distant comets were first achieved for product species, including CO^+, N_2^+, and CN (Cochran et al. 1980, 1991; Cochran & Cochran 1991; Korsun et al. 2008; Knight & Schleicher 2015). Rauer et al. (2003) reported C_3 and CN in the coma of Hale-Bopp as far as 7.0 and 9.8 au, respectively.

Primary volatiles have been especially hard to detect in distant comets (see Womack et al. 2017 for a recent review). Radio techniques allowed for extensive spectral and spatial studies of CO in the coma of 29P/Schwassmann-Wachmann 1 (29P/SW 1; Senay & Jewitt 1994; Crovisier et al. 1995; Festou et al. 2001; Gunnarsson et al. 2002, 2008). These investigations reported both the temporal evolution of CO production rates and CO coma morphology. In the near-infrared, Paganini et al. (2013) detected a series of rovibrational lines of CO in 29P at $R_h = 6.26$ au and reported rotational temperatures, gas production rates, and the spatial distribution of CO emission (along the entrance slit). They also reported upper limits for seven additional molecules.

CO was first detected in Hale-Bopp at $R_h = 6.7$ au pre-perihelion (Biver et al. 1996; Jewitt et al. 1996). Biver et al. (2002) detected rotational transitions of CO out to 14 au post-perihelion, HCN and CH_3OH out to 6 au, and H_2S, CH_3CN, and H_2CO out to 3–4 au. In the infrared, CO was observed out to $R_h = 4.1$ au and C_2H_6 out to 3.0 au (DiSanti et al. 2001; Dello Russo et al. 2001; Mumma et al. 2003).

Comet C/2006 W3 (Christensen) provided the best opportunity for ground-based spectroscopy of "hypervolatiles" at $R_h > 3$ au since Hale-Bopp. These two comets bear a key similarity: their gaseous comae were CO-rich (Crovisier 1999; DiSanti et al. 1999; Brooke et al. 2003; Bockelée-Morvan et al. 2010). However, in sharp contrast to Hale-Bopp, in 2009 C/2006 W3 had a perihelion distance of 3.13 au, which is outside the zone where water production rates are expected to strongly dominate the outgassing. Korsun et al. (2016) searched for emissions of product species in this comet (pre-perihelion). While no emissions were detected between

* Based on observations collected at the European Southern Observatory, Cerro Paranal, Chile, programs 084.C-0332, 084.C-0342, and 285.C-5006.

Table 1
Comet C/2006 W3 (Christensen): Observing Log

UT Date [yyyy mm/dd.dd][a]	R_h[b] [au]	dR_h/dt[b] [km s^{-1}]	Δ[b] [au]	$d\Delta/dt$[b] [km s^{-1}]	Phase Angle	Searched Species	Time on Source [minutes]
2009 Oct/07.01	3.252	+4.6	3.00	+36.0	18°	C_2H_6; CH_4	32
2009 Oct/07.08	3.252	+4.6	3.00	+36.1	18°	CO	32
2009 Oct/08.01	3.255	+4.6	3.02	+36.2	18°	C_2H_6; CH_4	16
2009 Oct/08.03	3.255	+4.6	3.02	+36.2	18°	CO	16
2010 Mar/31.41	4.029	+9.9	4.27	−20.7	13°	CO	16
2010 Apr/01.41	4.035	+10.0	4.26	−20.9	14°	CO	32
2010 Jul/23.28	4.734	+11.3	3.88	+26.2	7°	CO	32
2010 Jul/23.30	4.734	+11.3	3.88	+26.3	7°	C_2H_6; CH_4	20
2010 Jul/24.21	4.740	+11.3	3.89	+26.8	7°	CO	16
2010 Jul/25.15	4.746	+11.3	3.91	+27.3	8°	CO	16
2010 Jul/26.24	4.753	+11.3	3.92	+27.8	8°	C_2H_6; CH_4	24

Notes.
[a] All dates are post perihelion.
[b] R_h and Δ are heliocentric and geocentric distance, respectively; dR_h/dt and $d\Delta/dt$ indicate geocentric and heliocentric Doppler shift.

$R_h = 8.49$ and 6.25 au, several radicals (CN, C_3, C_2, CH, NH_2, and CO^+) were identified at $R_h = 3.74$ au.

In this paper, we report infrared detections of ethane (C_2H_6) and methane (CH_4) in comet C/2006 W3 at $R_h = 3.25$ au post-perihelion. The infrared provides a unique spectral window to study both species, since these symmetric hydrocarbons do not have allowed pure rotational transitions. We also report infrared detections of CO at $R_h \approx 3.25$, 4.0, and 4.7 au. Since CO and CH_4 sublimate at very low (and similar) temperatures (provided they are not trapped in less volatile ices), a comparison of their outgassing rates can assist in assessing the main driver of nucleus activity. We discuss our results in the context of other studies of comet C/2006 W3, including pre-perihelion observations by Japan's Infrared Satellite *AKARI* (Ootsubo et al. 2012) and post-perihelion measurements using the *Herschel Space Observatory*, complemented by ground-based radio facilities (Bockelée-Morvan et al. 2010; de Val-Borro et al. 2014). We also compare our $C_2H_6/CH_4/CO$ abundance ratios measured in the coma of C/2006 W3 with those in other comets observed well outside, near the limit, and well inside the zone of fully activated water sublimation.

2. Observations of Comet C/2006 W3 (Christensen) at ESO/VLT

E. J. Christensen discovered comet C/2006 W3 on Catalina Sky Survey images taken on UT 2006 November 18.4 at a heliocentric distance of 8.7 au. Several ground-based observers confirmed the appearance of a diffuse, slightly elongated coma shortly after the discovery (Christensen et al. 2006, IAU Circular 8777). Nakano (2011) computed the inverse original semimajor axis ($1/a_0 = 0.0003671$), suggesting the comet is not dynamically new; an inclination of 127.°07; and a perihelion distance for the 2009 apparition of $q = 3.1262$ au. Its Tisserand parameter ($T_j \sim -1.32$) dynamically links C/2006 W3 to the Oort cloud reservoir.

We observed C/2006 W3 using the Cryogenic Infrared Echelle Spectrograph (CRIRES; Käufl et al. 2004) at ESO's Very Large Telescope (VLT) Observatory atop Cerro Paranal, Chile. A slit width of 0.″4 (5 pixels) resulted in a spectral resolving power $\lambda/\delta\lambda \approx 55{,}000$. Emission from hypervolatiles was targeted near 3.3 μm (CH_4, C_2H_6) and 4.6 μm (CO). Three observing runs were conducted post-perihelion, at $R_h \approx 3.25$–3.26, 4.03–4.04, and 4.73–4.75 au (Table 1). Observations near 3.25 au and 4.7 au were conducted in visitor observing mode, while those near 4.0 au used the VLT queue observing mode and were restricted to CO owing to the limited time available. Observations at 4.7 au were acquired under Director's Discretionary Time.

The most valuable data are those from $R_h = 3.25$ au. These spectra revealed emissions from all three targeted hypervolatiles and returned a wealth of spatial information measured along the spectrometer's long entrance slit. The data at $R_h \approx 4.7$ au contain very limited spatial information, but provided significant upper limits for the abundance ratios of C_2H_6 and CH_4 relative to CO.

At 3.25–3.26 au, 4.73 au, and 4.75 au, non-sidereal tracking on the comet was achieved by locking the Adaptive Optics (AO) system on the central brightness condensation of the coma and/or by differential auto-guiding relative to a nearby star. Although the observations at $R_h = 4.03$–4.04 au and 4.74 au were made in "open loop" (non-AO) execution, these data also permitted us to derive reliable production rates.

3. Extracted Spectra and their Interpretation

Algorithms for data reduction and spectral analysis are detailed elsewhere (Bonev 2005; DiSanti et al. 2006, 2016; Lippi 2010; Villanueva et al. 2011a, and references therein) and have been successfully applied to previous CRIRES data on comets (Boehnhardt et al. 2008; Villanueva et al. 2009; Paganini et al. 2012, 2013; Lippi et al. 2013). We found that the near-infrared continuum (linked to reflected sunlight and/or thermal emission from micrometer-sized dust) in C/2006 W3 was extremely weak and the flux was heavily dominated by molecular rovibrational emissions.

Figure 1 (Panels A and B) shows detections of C_2H_6 (in the ν_7 vibrational band) and CH_4 (in the ν_3 band) at $R_h = 3.25$ au. While C_2H_6 was detected in Hale-Bopp at a similar heliocentric distance ($R_h = 3.0$ au, see Section 1), the detection of CH_4 in C/2006 W3 sets (by far) a new distance record for identifying methane in a comet by ground-based astronomical remote sensing. CH_4 was detected at 1.7 au in C/1999 T1 (McNaught-Hartley) (Gibb et al. 2003), at 2.03 au in C/2009 P1 (Garradd) (Paganini et al. 2012), and at 2.51 au in C/2010 G2 (Hill) (Kawakita et al. 2014).

Figure 1 (Panels C-E) shows CO lines (in the 1-0 band) detected at 3.25, 4.04, and 4.73 au, respectively. The R0 line of CO at ~2147 cm^{-1} (Figure 1(C)) was excluded from

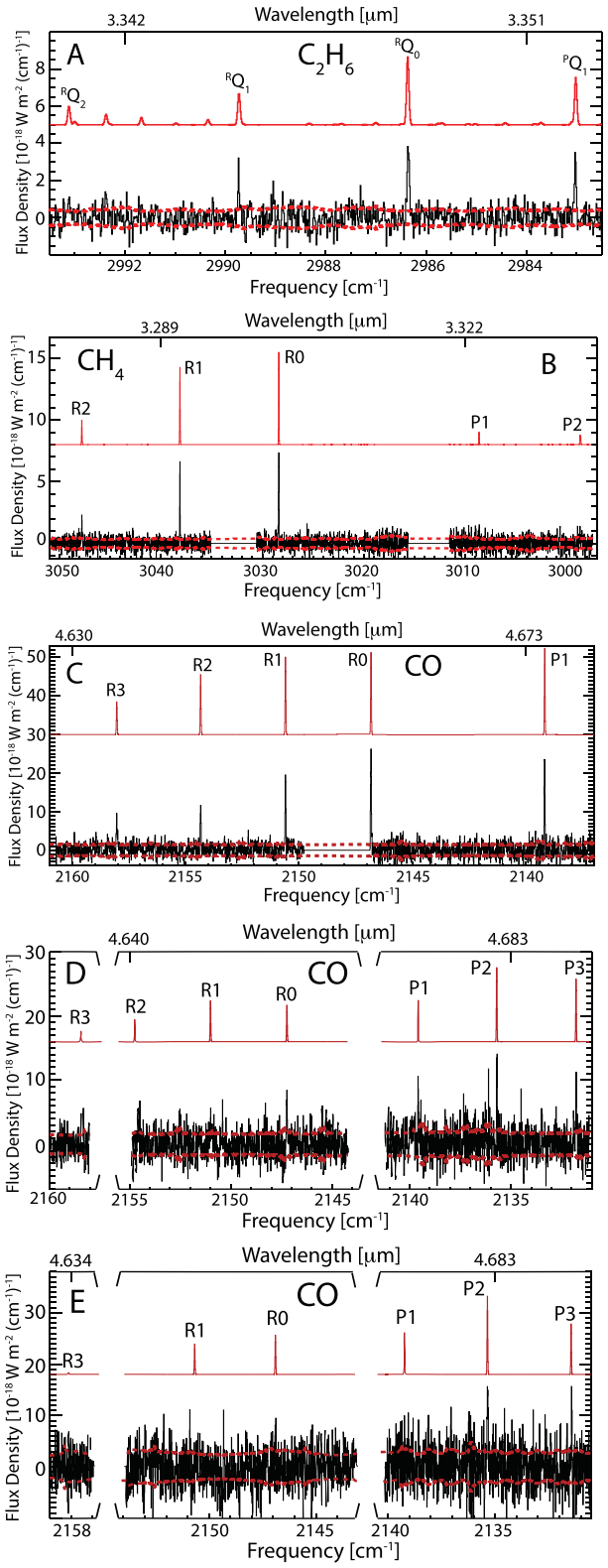

Figure 1. Spectra of hypervolatiles in comet C/2006 W3 Christensen. Panels (A, B, and C) show emission of C_2H_6, CH_4, and CO, respectively, at $R_h = 3.25$ au (UT 2009 October 7). Panel (D) shows emission of CO at $R_h = 4.04$ au (UT 2010 April 1), while Panel (E) shows emission of CO at $R_h = 4.73$ au (UT 2010 July 23). In each panel the ranges without spectral content indicate the gaps in frequency space between CRIRES detectors. Modeled emissions are shown in red above each extracted spectrum (see Section 3). Individual rotational transitions are labeled above each model. Some of these transitions (Panel B: R0 and R1 for CH_4; and Panel C: P1, R0, R1, R2, and R3 for CO) are discussed in Sections 3 and 4.2 in the main text.

quantitative analysis because it falls at the edge of a CRIRES detector, where our data reduction algorithm does not provide a sufficiently accurate measure of line flux. However, excluding this single line did not affect the subsequent analysis, since several other CO emissions are detected with high signal-to-noise ratios (S/N). We modified the spectral setting for the observations at 4.0 and 4.7 au, shifting the R0 line away from the edge of the detector. Although noisier, CO emissions are clearly present in the spectra at $R_h = 4.0$ au (Figure 1(D)). Only the P3 and P2 lines of CO are identified at $R_h = 4.7$ au (Figure 1(E)). Detections of weaker CO lines are not expected given the stochastic noise envelope ($\pm 1\sigma$) denoted by dashed red lines in this spectrum.

Modeled emissions are shown above each extracted spectrum. The modeled line intensities scale as the product of fluorescence efficiency (g-factor) and terrestrial atmospheric transmittance for Paranal conditions at the time of the observations. We used the LBLRTM spectral transmittance models (Clough et al. 2005; Villanueva et al. 2011a) to account for the wavelength-dependent telluric absorption of cometary flux. The comet's favorable geocentric Doppler shifts (Table 1) offset its CH_4 and CO lines from their (opaque) terrestrial counterparts into regions of high atmospheric transmittance. The analysis of C_2H_6 is generally much less sensitive to Doppler shift owing to the weakness of terrestrial C_2H_6 features. For all three molecules, the transmittance modeling is not a significant source of uncertainty in establishing production rates.

We used modeled fluorescence g-factors [photons s^{-1} molecule^{-1}] for CH_4 (Gibb et al. 2003), C_2H_6 (Villanueva et al. 2011b), and CO (Paganini et al. 2013). These g-factors assume optically thin conditions. We also used newly developed g-factors for CO and CH_4 from G. L. Villanueva et al. (2017, in preparation). These new g-factors agree with the aforementioned fluorescence models for optically thin conditions, but also account for optically thick infrared emission, in combination with using the long-slit capability of CRIRES. Because this new work is not yet published, we describe in the Appendix our formalism in sufficient detail for the present analysis.

4. Spatial Distributions at 3.25 au

4.1. The Importance of Using Long-slit Capability

The spectra acquired at $R_h = 3.25$ au have the highest S/N. This permits examining how directly measured quantities (emission line intensity, Section 4.2) and retrieved quantities (column density, Section 4.3, and symmetric production rate, Section 4.4) vary with offset distance from the nucleus along the entrance slit. This ability to extract detailed spatial information was vital for identifying those lines of sight through the coma from which the emission is optically thick, and hence where the resulting production rates are most affected by uncertainties and parameters we cannot constrain from our observations. For our reported production rates we then use only the signal from those regions of the coma that were minimally affected by optical depth.

4.2. Spatial Profiles of Emission Intensity: Hydrocarbons versus CO

We measured the spatial intensity distribution of individual lines of CO and CH_4 at 3.25 au. The spatial profiles of the R1

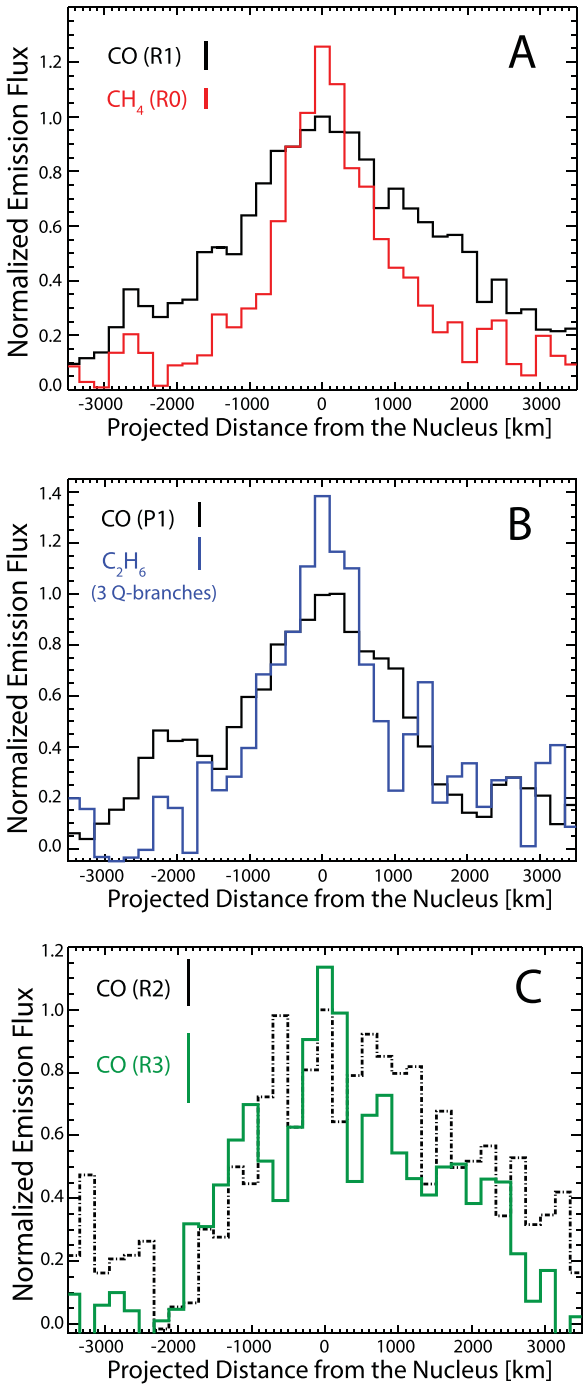

Figure 2. Spatial profiles of the *measured emission intensity* along the slit. The unresolved nucleus corresponds to the zero-point of the *x*-axis. The comet was observed in "elevation mode," meaning that the slit was maintained at the parallactic angle (≈139° for the hydrocarbons setting, and at ≈121° for the CO setting). A meaningful comparison between spatial profiles in each panel requires placing them on the same vertical scale. The *y*-axis is first normalized so the peak flux is 1.0 for the R1, P1, and R2 line of CO for panels A, B, and C, respectively. The profiles are then scaled based on the signal in their central five pixels. Stochastic uncertainties (1σ) per spatial pixel are shown next to the color legend for each spatial profile (upper left corner of the plot).

and R0 lines of CH_4 are nearly identical, but CO exhibits a different spatial behavior, both to CH_4 and also among CO lines. Figure 2(A) compares profiles of the CO (R1) and CH_4 (R0) lines. While the CH_4 distribution is strongly peaked near the nucleus, the profile of CO is flatter in its central portion and decreases more slowly away from the nucleus than that of CH_4.

Since the C_2H_6 lines were generally weaker, we combined spatial profiles for the three strongest emissions (ν_7 Q-branches), which we compare with that of CO (P1) in Figure 2(B). A similar spatial behavior is revealed: like methane, the more narrowly peaked ethane emission contrasts with the flatter distribution of CO. Finally, we compare the profiles of the CO R2 and R3 emissions in Figure 2(C).

What causes the different spatial behavior of CO emission when compared to methane and ethane? We consider two possibilities, and examine each in turn:

1. CO was released (at least in part) from an extended source in the coma, while methane and ethane were released solely from the nucleus, and/or
2. optical depth effects reduced the apparent flux near the nucleus, but more so for CO than for either hydrocarbon.[7]

The flattened appearance of CO profiles could be due to extended source production (e.g., Womack et al. 2017). Direct release of volatiles (CH_4, C_2H_6, CO_2, and CO itself) from the nucleus could also drag ice into the coma, similar to the release of H_2O icy clumps (and grains) from 103P/Hartley 2 (A'Hearn et al. 2011; Mumma et al. 2011; Bonev et al. 2013; Fougere et al. 2013; Protopapa et al. 2014). In this scenario, a flattened spatial profile would be consistent with CO-rich clumps subliming slowly while transiting the region within the ∼1000 km from the nucleus that is covered by our CRIRES observations. However, the observed spatial profiles do not suggest extended release of methane and ethane. Of the three molecules we measured in C/2006 W3, CO has the lowest sublimation temperature. If CO-rich ice survived in the coma, we would expect CH_4 and C_2H_6 ices to also survive and thus their emissions to exhibit similarly broad spatial distributions. Although we cannot completely rule out production of CO from an extended source, the observed narrower profiles of methane and ethane argue against extended release of hypervolatiles.

As an alternative to a dominant release of CO from icy grains, the flattened appearance of the CO profiles is also consistent with optically thick conditions for lines of sight passing close to the nucleus (i.e., the central parts of the intensity distributions shown on Figures 2(A)–(C)). We quantitatively explore this possibility in the next section.

4.3. Retrieved Spatial Profiles of Column Density

We retrieved the spatial profiles of column density (N) by performing a Levenberg-Marquardt χ^2 fit of modeled to measured spectra (e.g., Figure 1). This method is detailed in Villanueva et al. (2008) and Bonev et al. (2013). The quality of the fit depends on the mean rotational temperature ($T_{\rm rot}$)[8] for a given field of view (FoV). For a nucleus-centered aperture of 5 spectral × 5 spatial pixels (870 km × 935 km at the geocentric distance $\Delta = 3.00$ au, see Table 1), we found $T_{\rm rot} = 20^{+6}_{-4}$ K for

[7] Another mechanism for extended CO production could be photolysis of CO_2 and/or H_2CO. However, the photodissociation decay scale lengths of both species are expected to exceed (by far) the observed spatial scale for comet C/2006 W3 at $R_h = 3.25$ au. Similarly, dissociative production of CO by electron impact on CO_2 or H_2CO would require far higher production rates than were observed in this comet.

[8] This effective temperature is defined as a weighted (by local number density) mean over the line of sight, as prescribed by Fougere et al. (2012).

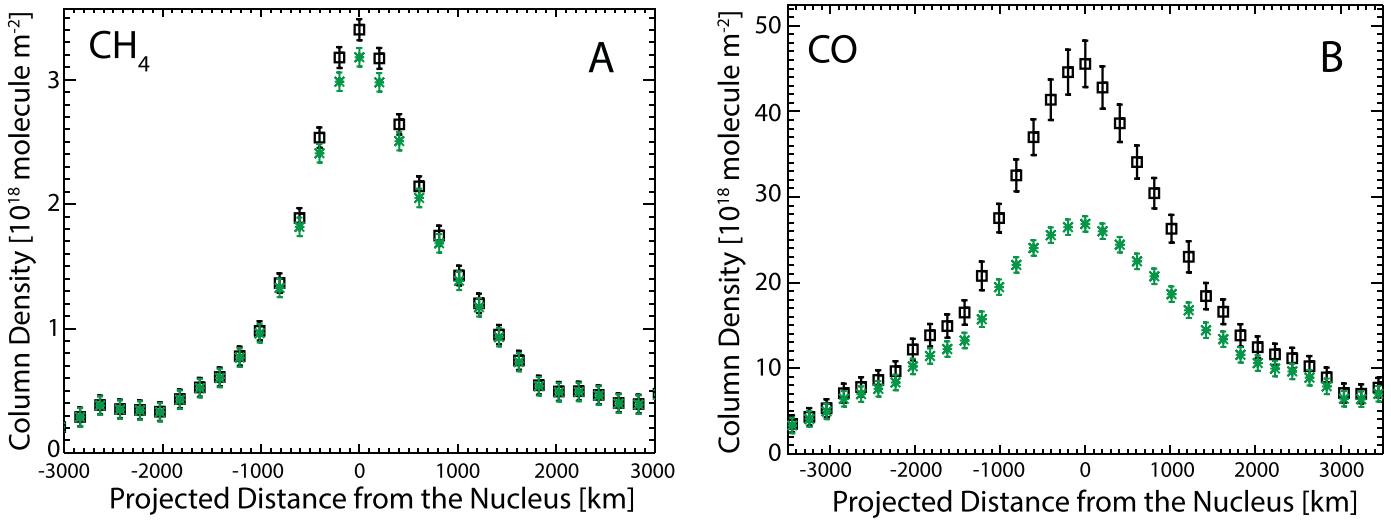

Figure 3. Spatial profiles of retrieved column density for CH_4 (Panel A) and CO (Panel B). In each panel, green stars indicate retrievals using the optically thin g-factors, while black squares show the results from a curve-of-growth analysis, which includes optical depth effects. Each column density retrieval corresponds to a rectangular aperture of 3 pixels (along the slit) × 5 pixels (1 slit width).

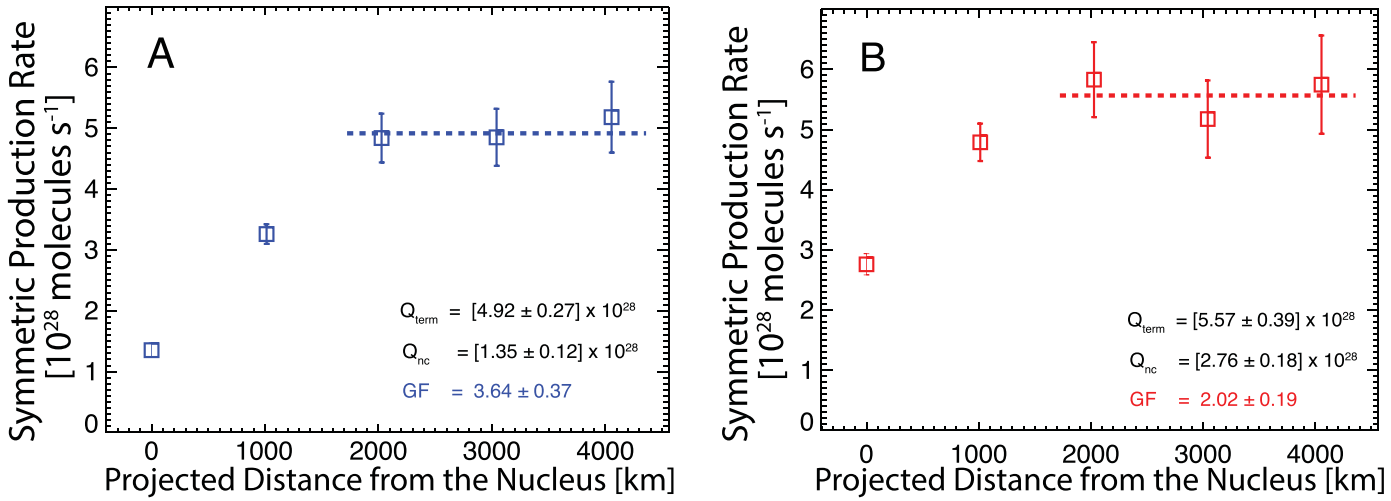

Figure 4. Q-curves showing retrieved symmetric production rate of CO vs. cometocentric distance. Panel (A): assuming optically thin conditions. Panel (B): assuming optically thick conditions. Nucleus-centered production rate (Q_{nc}), terminal production rate (Q_{term}), and resulting growth factor (GF) are indicated in each graphic. Each Q_{term} is a weighted mean of individual production rates for the "leveled" part of the Q-curve, marked with a dashed line. The terminal production rates (Panels A and B) agree within uncertainty.

C_2H_6 (Figure 1(A)), $T_{rot} = 16 \pm 3$ K for CH_4, (Figure 1(B)), and $T_{rot} = 14 \pm 2$ K for CO (Figure 1(C)). Our spectra did not allow for detecting any significant variation in T_{rot} along the slit. However, the retrieved column density (and production rate) is very insensitive to T_{rot} for the realistic range of ~10–25 K. Therefore, for the simulations shown in this section, we fixed T_{rot} at 16 K. We verified that assuming another fixed value within 10–25 K or a gradient in T_{rot} along the slit did not alter the retrieved profile of N in any significant way. For example, when T_{rot} was varied (as a parameter) from 10 K to 20 K, the column density in the central FoV changed by less than 2σ uncertainty.

Figures 3(A) and (B) show the spatial distributions of the column density for CH_4 and CO, respectively. The column density is based on a χ^2 fit to all emissions, which is significantly less sensitive to spatial fluctuations of individual line intensities. Because this fit encompasses multiple lines, our profiles of the column density are smoother in appearance than those in Figures 2 (A)–(C), which pertain to individual line fluxes.

Each panel of Figure 3 shows two column density curves: green stars indicate retrievals using optically thin g-factors, while black squares show the results from a curve-of-growth analysis (Appendix), assuming that optical depth reduces the local pump intensity within the column and thus also the effective fluorescence efficiency. If optical depth is important, we expect the two column density curves (green stars and black squares) to diverge. This is not the case for Figure 3(A), suggesting that the CH_4 emission is nearly optically thin even in the center of the spatial profile. Conversely, Figure 3(B) suggests that optical depth significantly affects the CO emission in the central parts of the profile, consistent with the flatter appearance of the distributions of CO emission intensity, compared with those of CH_4 (and C_2H_6).

4.4. The Spatial Distribution (Q-curve) of Symmetric Production Rates for CO

Figure 4(A) shows how the *retrieved*[9] symmetric production rate ($Q_{\rm sym}$, molecules s^{-1}; Mumma et al. 2003) of CO varies with projected distance from the nucleus (ρ, km), assuming optically thin conditions. Conversely, Figure 4(B) shows how $Q_{\rm sym}$ varies with ρ when optical depth is included. The $Q_{\rm sym}$ (ρ) graphical relationship is commonly referred to as a "Q-curve" (Dello Russo et al. 1998; DiSanti et al. 2001; Bonev et al. 2006; Villanueva et al. 2011a; Paganini et al. 2013). Each value of $Q_{\rm sym}$ in Figures 4(A) and (B) was derived from measured column densities $\langle N \rangle$ according to the relationship:

$$Q_{\rm sym} = \frac{\langle N \rangle \, A_{\rm FoV}}{t\,(R_h)\, f\,(x)}. \quad (1)$$

In Equation (1), $A_{\rm FoV}$ (m^2) represents the "footprint" area corresponding to a rectangular aperture of 5 spectral pixels (the slit width) × 5 spatial pixels (870 × 935 km); $t(R_{\rm h})$ (s) is the photodissociation lifetime of CO ($t(R_{\rm h}) = t(1\,{\rm au})\ R_{\rm h}^2$, where $t(1\,{\rm au}) = 1.3 \times 10^6$); and $f(x)$ represents the fraction of all CO molecules that are sampled within the FoV. Spherically symmetric uniform outflow is assumed; see Yamamoto (1982) and the Appendix of Hoban et al. (1991). Since $f(x)$ varies as approximately t^{-1} for CO given our beam size, the product of t and $f(x)$, and hence the extracted production rate is relatively insensitive to the adopted lifetime. However, $f(x)$ depends directly on gas outflow velocity ($v_{\rm exp}$, as discussed in Appendix). Importantly, for off-nucleus extracts, the column density $\langle N \rangle$ is the *mean* of two measurements obtained from FoVs equidistant from the peak intensity on opposite sides of the spatial profile. This approach minimizes the effects of possible asymmetries in the gas outflow (Xie & Mumma 1996); hence the term *symmetric* production rate.

Figure 4 shows that the retrieved symmetric production rates initially increase with projected distance (ρ) from the nucleus until a "terminal" value is reached at $\rho \sim 1800$ km. Each Q-curve is characterized by three quantities: the nucleus-centered production rate ($Q_{\rm nc}$), the "terminal" value ($Q_{\rm term}$), and the distance from the nucleus required to reach $Q_{\rm term}$. The ratio $Q_{\rm term}/Q_{\rm nc}$ is commonly referred to as the "growth factor" (GF). In comparing the Q-curves that result from our optically thin (Figure 4(A)) and optically thick (Figure 4(B)) treatments we point out the following features:

1. The terminal production rates agree within the uncertainty.
2. If optically thin g-factors are adopted (Figure 4(A)), the nucleus-centered production rate is much lower than the rate we obtain using an optical depth treatment (Figure 4(B)).

In *both* Q-curves the initial rise in retrieved production rate is related to net loss of flux from the nucleus-centered region, primarily because of atmospheric seeing and (possibly) small guiding inaccuracies. However, when optically thin g-factors are applied to an optically thick medium (Figure 4(A)), the nucleus-centered production rate is further underestimated (well beyond that caused by loss due to seeing) by (wrongly) assuming that the retrieved column density is directly proportional to the measured flux. Since optical depth effects are most significant at the peak intensity of the spatial distributions, the difference in the corresponding production rates is largest for the nucleus-centered extract.

[9] Note that there is a distinction between retrieved symmetric production rates (based on the fluxes in successive fields of view) and the "true" (best estimate) production rate for the outgassing of the volatile; the latter requires a Q-curve analysis, as described in this section.

5. Production Rates of CO, CH_4, and C_2H_6 at 3.25, 4.0, and 4.7 au

Table 2 summarizes all production rates obtained in this study with the following considerations:

1. The agreement in terminal production rates based on optically thick and optically thin treatments is consistent with optical depth minimally affecting emissions in the wings of the spatial profiles of CO (i.e., for lines of sight away from the nucleus). We therefore consider $Q_{\rm term}$ in Figure 4(B) as the most reliable measure of CO gas productivity. The data obtained at $R_{\rm h} \approx 3.25$ au and 4.0 au permitted extracting spectra at successive positions along the slit, analyzing (line-by-line) each spectrum individually, and obtaining reliable Q-curves.
2. In contrast to CO, the hydrocarbon (CH_4, C_2H_6) emissions peak strongly at the nucleus and decrease more rapidly with increasing nucleocentric distance, precluding sufficient S/N to obtain reliable Q-curves. From these emissions we obtained nucleus-centered production rates from Equation (1). To obtain a terminal production rate, we then multiplied $Q_{\rm nc}$ by an empirical growth factor correction that accounts for slit losses alone. This correction was derived from a simplified Q-curve, obtained not by analyzing individual emissions, but by summing the fluxes of several lines to increase the S/N, and assuming a constant g-factor along the slit. This is the most common approach in infrared studies. It has been tested against "true" Q-curves and provides an excellent approximation in the optically thin case.
3. The CO data at $R_{\rm h} = 4.73$–4.75 au contain no significant spatial information because of reduced gas productivity and because those data were obtained with 5″ (versus 15″ for the other two observing runs) beam separation. The emissions are close to the optically thin case, and an empirical growth factor was derived from the data obtained on UT 2010 July 23 and 25 (see Table 2). The data from July 24 do not permit a measure of growth factor, and this introduces additional uncertainty into our analysis. We therefore conservatively assume a wide (but realistic) range for GF (1.7–4.0). We calculated Qs for the lower and upper bound of this range, adopted their mean value ($1 \times 10^{28}\ s^{-1}$), and propagated the GF-dominated uncertainty into our reported terminal production rate.
4. In the three observations near 4.7 au, individual lines of CO were detected only on July 23 (Figure 1(E)), when the time on source was longest. On July 24 and 25, only tentative detections of CO were achieved by summing the fluxes of all sampled lines as described in Villanueva et al. (2009). These Qs for CO at 4.7 au therefore have a larger uncertainty (independent of GF), but are nonetheless useful for constraining the decrease in CO gas production with increasing heliocentric distance. The production rates, measured at three different dates near $R_{\rm h} = 4.7$ au are in good agreement.

Table 2
Production Rates in Comet C/2006 W3 (Christensen) as a Function of Heliocentric Distance

R_h [au]	T_{rot} [a] [K]	Q_{nc} [b] [10^{27} s^{-1}]	Q_{term} [c] [10^{27} s^{-1}]	Growth Factor (GF)
		Carbon Monoxide (CO)		
3.252	14 ± 2	27.6 ± 1.8	55.7 ± 3.9	2.02 ± 0.19[d]
3.255	11^{+2}_{-1}	28.2 ± 2.4	55.2 ± 3.3	1.95 ± 0.20[d]
4.029	(7)	4.7 ± 1.6	19.0 ± 2.5	4.04 ± 1.48[d]
4.035	7^{+2}_{-1}	9.2 ± 1.8	16.1 ± 1.7	1.75 ± 0.38[d]
4.734	(7)	7.1 ± 1.9	12.1 ± 3.5	1.7 ± 0.2[e]
4.740	(7)	3.5 ± 0.9	10.0 ± 4.0	(1.7); (4.0)[f,g]
4.746	(7)	3.2 ± 1.0	13.4 ± 5.1	4.2 ± 0.9[e]
		Methane (CH_4)		
3.252	16 ± 3	1.71 ± 0.05	2.68 ± 0.28	1.57 ± 0.16[e]
3.255	22 ± 5	1.73 ± 0.10	2.20 ± 0.26	1.27 ± 0.13[e]
4.734	(7)	<0.7 (3σ)	<1.2 (3σ)	(1.7)[f]
4.753	(7)	<0.5 (3σ)	<0.8 (3σ)	(1.7)[f]
		Ethane (C_2H_6)		
3.252	20^{+6}_{-4}	0.78 ± 0.04	1.23 ± 0.14	1.57 ± 0.16[e]
3.255	(22)	0.88 ± 0.07	1.11 ± 0.14	1.27 ± 0.13[e]
4.734	(7)	<0.4 (3σ)	<0.6 (3σ)	(1.7)[f]
4.753	(7)	<0.3 (3σ)	<0.5 (3σ)	(1.7)[f]

Notes.
[a] Effective rotational temperature for the nucleus-centered region. Values in parenthesis are assumed. In these cases, the resulting production rates and (especially) the C_2H_6/CH_4 /CO abundance ratios change insignificantly when T_{rot} is varied by ~10 K.
[b] The nucleus-centered production rate is based on integrating the signal over 5 spatial pixels for 3.25 and 4.0 au and 15 spatial pixels for 4.7 au.
[c] "Terminal" production rate.
[d] GF is based on a full Q-curve analysis, as described in Section 4.4.
[e] Empirical growth factor, based on summing the flux of individual lines (see Section 5).
[f] GF values in parenthesis are assumed.
[g] Since there is no spatial information on that date (affected by heavy and variable cirrus conditions), two values that bracket a representative range of GF are assumed. We calculated Qs for both GF, adopted their mean value (10.0×10^{27} s^{-1}), and propagated the GF-dominated uncertainty into the reported terminal production rate

6. Discussion

6.1. C/2006 W3 Christensen as Seen at Different Wavelengths

The vast majority of molecular studies in comets have been restricted to heliocentric distances smaller than 2 au, where H_2O has the highest production rate among volatiles (Mumma & Charnley 2011; Dello Russo et al. 2016). In contrast, C/2006 W3 (Christensen) remained outside $R_h = 3.1$ au throughout its apparition, but its exceptional brightness presented an extremely rare opportunity to sense a suite of primary volatiles. This comet was observed from several space- and ground-based facilities. As a part of its 18-comet survey (Ootsubo et al. 2012), Japan's infrared satellite *AKARI* observed C/2006 W3 pre-perihelion with low spectral resolution but wide spectral coverage (2.5–5 μm). These studies focused on CO_2, whose IR band at 4.3 μm was detected simultaneously with bands of H_2O and CO. Observations of C/2006 W3 near 3.3 au were among the first science highlights of the *Herschel Space Observatory*, complemented by ground-based programs at Nančay and the IRAM radio telescopes (Bockelée-Morvan et al. 2010; de Val-Borro et al. 2014).

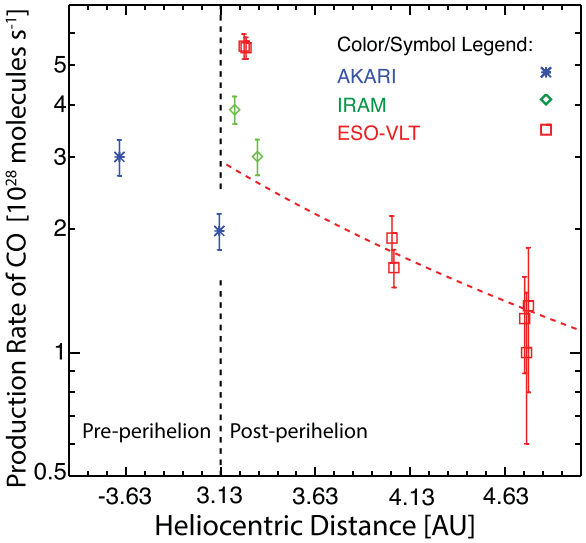

Figure 5. CO production rates as measured by IRAM (green diamonds, Bockelée-Morvan et al. 2010), *AKARI* (blue stars, Ootsubo et al. 2012), and ESO-VLT (red squares, this work). *AKARI* and VLT results are based on infrared measurements of the CO 1-0 band vibrational emissions, while IRAM results are based on measurements of the velocity-resolved CO (2-1) rotational line. The red dashed line corresponds to insolation-limited (R_h^{-2}) production rates.

Figure 5 shows a compilation of CO production rates in C/2006 W3 measured by *AKARI*, IRAM, and ESO-VLT. The post-perihelion production rates measured near 4.0 and 4.7 au are consistent with insolation-limited outgassing ($Q \propto R_h^{-2}$), while a steeper decrease is observed between 3.2 and 4.0 au (see also Table 2). For $R_h < 3.35$ au, the reported production rates span the range ~2.0 to 5.5 (10^{28} molecules s^{-1}). Regardless of differences among individual measurements, these CO production rates are higher in C/2006 W3 than those measured in most previously studied comets, although these previous comets were observed significantly closer to the Sun.

Our two measurements ($R_h = 3.25$ au; 2009 October 7 and 8) are in agreement, but are ~1.4 times higher than Q(CO) from IRAM ($R_h = 3.20$ au; 2009 September 14) and ~2.8 higher than Q(CO) from *AKARI* ($R_h = 3.13$ au; 2009 June 16). The presented measurements (which are weeks to months apart) are based on three very different techniques. Ootsubo et al. (2012) discuss that systematic uncertainties (e.g., due to different beam sizes) and modeling assumptions behind each technique can partly account for differences among the production rates (see also Dello Russo et al. 2009; Magee-Sauer et al. 1999). We note that differences in Q(CO) are not related to the assumed gas outflow velocity. Both infrared studies (ESO-VLT and *AKARI*) adopt similar values (~440 m s^{-1}) of this parameter, in agreement with IRAM's measurements based on velocity-resolved rotational lines. Temporal variability in Q(CO) between the time of *AKARI* observations and those of ESO-VLT (~4 months later) cannot be ruled out. *AKARI*'s observations alone suggest a ~30% decrease in Q(CO) from $R_h = 3.66$ to $R_h = 3.13$ au (pre-perihelion). In addition, *AKARI* observed the same infrared band as was targeted in our measurements, but at much lower spectral resolution. Q(CO) was then calculated assuming optically thin conditions and a band-integrated g-factor: $g_{band} = 2.6 \times 10^{-4}$ s^{-1}. For heliocentric radial velocity near zero (corresponding to *AKARI*'s observation near perihelion),

our optically thin model predicts $g_{\rm band} \approx 1.2$ to 1.5×10^{-4} s^{-1}, depending on rotational temperature (Paganini et al. 2013; Villanueva et al. 2012; see also Goddard's Planetary Spectrum Generator; http://ssed.gsfc.nasa.gov/psg/). This difference in $g_{\rm band}$ accounts for most of the difference between CRIRES and ESO-VLT measurements. *AKARI*'s lower value (3.13 au) is also consistent with optically thick CO, as suggested by our analysis at $R_{\rm h} = 3.25$ au. Although we expect *AKARI*'s very large FoV ($\sim 43''$) would diminish the influence of optical depth effects in their beam, their spatially integrated flux measurements might still include some contribution from the innermost (optically thick) regions of the coma, because CO column densities are highest near the nucleus.

A further and detailed comparison between the IRAM, *AKARI*, and ESO-VLT retrieval methods of Q(CO) is beyond the scope of this paper. Despite differences in productions rates (near perihelion) each of these studies brings unique and important insights: *AKARI* was essential as a window to CO_2 (not observable from the ground). *AKARI* results also helped in interpreting the imaging study by *Spitzer* (Reach et al. 2013) and the sources of forbidden OI emission detected from the Apache Point Observatory (McKay et al. 2012). Both investigations can be used to deduce the CO_2 production rate, but depend critically on knowledge of the CO/CO_2 ratio. Radio techniques were especially valuable for sensing a suite of volatiles (CO, CH_3OH, HCN, and H_2S, and CS) and of dust, for directly measuring gas outflow velocities, and for estimating the comet's comparatively large nucleus size ($\sim$20 km). Importantly, the HIFI instrument (*Herschel*) detected rotational emission from H_2O at 5 au from the Sun. ESO-VLT is essential for symmetric hydrocarbons (CH_4 and C_2H_6) and brings the best constraints on the post-perihelion decrease of the CO production rate with increasing $R_{\rm h}$, since all other measurements of CO are clustered within $R_{\rm h} < 3.35$ au. Synergistic interpretation of all these measurements provides the most in-depth view possible of the activity and composition of C/2006 W3.

6.2. Relative Abundances in the Coma

Relative abundances (CH_4/CO, HCN/CO, etc.) often provide a better representation of coma composition than absolute production rates. Figure 6 shows the abundances of several molecules with respect to CO. This molecule is chosen as a baseline because, first, it is the species with the highest production rate, and second, CO was most frequently measured in C/2006 W3. For all species except H_2O ($R_{\rm h} = 5$ au) and NH_3, the abundance ratios X/CO are based on measurements with the same instrument and on the same date as for carbon monoxide; using contemporaneous measurements minimizes the effects of temporal variability. Using the same instrument-telescope combination also minimizes systematic uncertainties associated with and propagated from flux calibration and modeling parameters that are specific to the particular observing technique (Mumma et al. 2003; DiSanti & Mumma 2008; Ootsubo et al. 2012; Dello Russo et al. 2016).

The *AKARI* relative abundances suggest that the coma of C/2006 W3 (Christensen) was rich in both CO and CO_2. The measured CO/CO_2 ratio (2.3 ± 0.3 and 3.5 ± 0.5 at $R_{\rm h} = 3.13$ and 3.66 au, respectively) is the second highest (after 29P/SW 1) of all studied comets, including those observed beyond 2.5 au from the Sun. Regardless of $R_{\rm h}$, only upper limits for CO production, and hence CO/CO_2, were

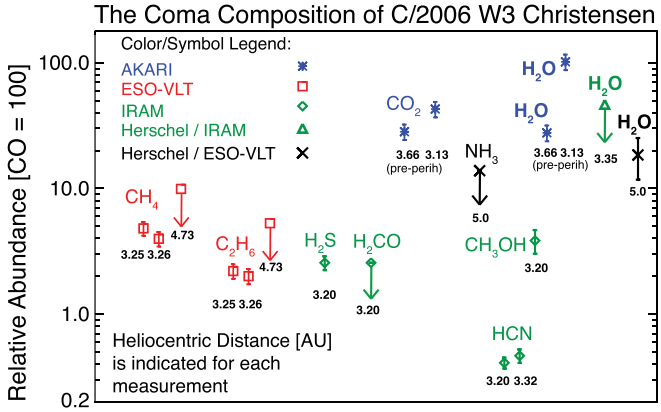

Figure 6. Abundances of species detected in comet C/2003 W3 (Christensen) relative to carbon monoxide based on de Val-Borro et al. (2014), Bockelée-Morvan et al. (2010), Ootsubo et al. (2012), and this work. Measurements from different observatories are marked according to the color/symbol legend in the top left corner of the figure and are explained in the main text (Section 6.2). Heliocentric distance is marked below each individual relative abundance. Unless explicitly indicated, abundances pertain to post-perihelion.

achieved in most other comets in the *AKARI* survey, making C/2006 W3 a definitive outlier given its high CO coma abundance.

Post-perihelion abundances of H_2O/CO and NH_3/CO cannot be obtained from a single instrument-facility, but are included in Figure 6, given the lack of coverage in these species in distant comets. The upper limit H_2O/CO (green triangle in Figure 6) is estimated from near-contemporaneous measurements by *Herschel* (H_2O; $R_{\rm h} = 3.35$ au) and IRAM (CO; $R_{\rm h} = 3.32$ au). We extrapolated our production rate of CO from 4.73 to 5.0 au assuming an $R_{\rm h}^{-2}$ dependence (as we observed between $R_{\rm h} = 4.0$–4.7 au; see above), and compared with $Q(H_2O)$ and $Q(NH_3)$ from *Herschel* (points marked with "x").

Overall, the revealed composition pertains to the coma at the time of observation, not necessarily to the bulk nucleus. The results summarized in Figure 6 provide a rare window to the coma abundances of primary volatiles in a distant comet. As such, they are especially valuable for constraining models for nucleus sublimation beyond $R_{\rm h} = 3$ au, where differences in volatility are very important, as demonstrated for C/2006 W3 Christensen by the nucleus outgassing model of Kossacki & Szutowicz (2015), which roughly reproduces our observed post-perihelion decrease in CO production rate in this comet.

6.3. Relative Abundances of C_2H_6, CH_4, and CO among Comets

Like CO, the production rates of C_2H_6 and CH_4 in C/2006 W3 exceed their respective values as measured in a number of comets that were observed significantly closer to the Sun. In C/2006 W3 at $R_{\rm h} = 3.25$ au, the three hypervolatiles scale approximately as $CO/CH_4/C_2H_6 = 100/4.4/2.1$. Table 3 compares these relative coma abundances to measurements in two other comets observed beyond 3 au from the Sun. The ratios CH_4/CO and C_2H_6/CO in C/2006 W3 at 3.25–3.26 au are consistent with the upper limits we report in C/2006 W3 at 4.73 au, and also with those reported for comet 29P/SW 1 at 6.26 au (Paganini et al. 2013).

Le Roy et al. (2015) detected methane, ethane, and carbon monoxide in the coma of comet 67P/Churyumov-Gerasimenko (67P) using the ROSINA mass spectrometer on board the

Table 3
Relative Abundances of the Hypervolatiles C_2H_6, CH_4, and CO in Comets Observed at $R_h > 3$ au

Comet	R_h[au]	Abundance			Technique	Reference
		C_2H_6	CH_4	CO		
	3.252	2.2 ± 0.3	4.8 ± 0.6	100	Remote sensing	This work
C/2006 W3	3.255	2.0 ± 0.3	4.0 ± 0.5	100		
	4.73	<5.0	<9.9	100		
67P/CG summer hem.[a]	3.15	11.9	4.8	100	in situ mass spectroscopy (~10 km from the nucleus)	Le Roy et al. (2015)
67P/CG winter hem.[a]	3.15	16.5	2.8	100		
29P/SW1	6.26	<2.2 (3σ)	<4.8 (3σ)	100	Remote sensing	Paganini et al. (2013)

Note.
[a] Le Roy et al. measured the following relative abundances of hypervolatiles and water: $C_2H_6/H_2O = 0.32$ (SH) and 3.3 (WH); $CH_4/H_2O = 0.13$ (SH) and 0.56 (WH); $CO/H_2O = 2.7$ (SH) and 20 (WH); "SH" and "WH" designate summer and winter hemisphere, respectively.

Rosetta space mission orbiter. The heliocentric distance of 67P (3.15 au) was very similar to that of our first observations of C/2006 W3 (3.25 au). However, the *Rosetta* in situ measurements reflect the local composition, approximately 10 km from the nucleus, rather than the line-of-sight-integrated composition afforded by remote-sensing measurements; this difference complicates a direct comparison with our results.

Emphasizing these caveats, Le Roy et al. nevertheless provided useful comparisons between the abundances of their detected species (relative to H_2O, which dominated 67P's outgassing) and those measured by ground-based telescopes in a number of comets within ~2 au from the Sun. Here we extend this effort by comparing hypervolatiles in 67P and C/2006 W3, which are the only two comets for which measurements at $R_h \approx 3.2$ au have been reported to date. In contrast to C/2006 W3 (which comes from the Oort cloud), 67P is an ecliptic (Jupiter-family) comet, most probably dynamically linked to the scattered Kuiper disk.

At the time of these *Rosetta* measurements, 67P was experiencing northern summer, with the northern pole in constant sunlight, while the southern pole was in permanent shadow. Le Roy et al. show that the abundances of each hypervolatile relative to H_2O differed by factors of ~4 (CH_4), ~10 (C_2H_6), and ~7 (CO) between the two hemispheres, with much lower X/H_2O ratios observed in the sunlit part of the coma (see Table 3, note a). Conversely, C_2H_6 /CO and CH_4/CO differed by less than a factor of 2 and followed the same trend, with ethane being more abundant than methane in both hemispheres. The in situ abundances of CH_4/CO in 67P are very similar to the column-integrated measurements in C/2006 W3, while C_2H_6/CO (and commensurately C_2H_6/CH_4) are distinctly higher.

Figure 7 includes 67P and C/2006 W3 in a diagram showing CO/CH_4 versus C_2H_6/CH_4 together with 17 comets observed between R_h of ~2.0 and 0.35 au (after Mumma & Charnley 2011; Paganini et al. 2014, and DiSanti et al. 2014, 2016). For these comets, water production rates strongly dominated those of all other species, so that their CO/H_2O ratios are color-coded. Except for 67P (a space mission target), all other comets in the figure are from the Oort Cloud; CH_4 and CO measurements are significantly underrepresented in ecliptic comets because of geocentric Doppler shift limitations. Both species were recently detected (along with C_2H_6) in the ecliptic comet 45P/Honda-Mrkos-Pajusakova, with preliminary ratios $CO/CH_4 \sim 1.0$ and $C_2H_6/CH_4 \sim 0.6$ (DiSanti et al. 2017; CBET 4357).

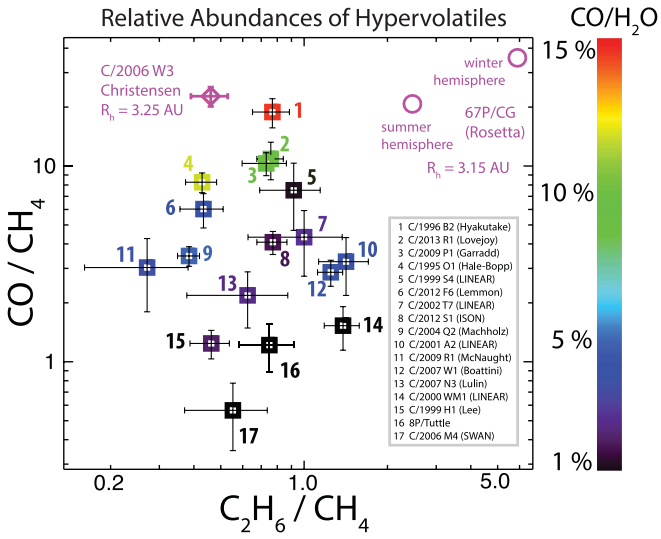

Figure 7. Diagram of CO/CH_4 vs. C_2H_6/CH_4 including comets C/2006 W3 (Christensen) (this work; $R_h = 3.25$ au), 67P/Churyumov-Gerasimenko (Le Roy et al. 2015; $R_h = 3.15$ au), and 17 comets observed between R_h of 2 au and 0.35 au (after Mumma & Charnley 2011; Paganini et al. 2014, and DiSanti et al. 2014, 2016). The value for C/2006 W3 is based on independent measurements on two different dates, which are in agreement (Table 3). Note that the 67P ratios are based on in situ mass spectroscopy (see Section 6.3) and therefore their interpretation against line-of-sight-integrated remote-sensing measurements is not straightforward. Each comet observed inside $R_h \sim 2$ au is numbered according to the legend inserted in a gray box in this graphic. The CO/H_2O ratio for these comets is color-coded. Importantly, the CO/H_2O ratio in C/2009 P1 (point 3) increased with time, reaching ~60% as the comet approached 2 au post-perihelion (Feaga et al. 2014).

The scatter in the diagram showing CO/CH_4 versus C_2H_6/CH_4 is consistent with recent correlation analyses of infrared measurements by Dello Russo et al. (2016). These authors report correlation coefficients of 0.49, 0.71, and 0.18 between CO and CH_4, C_2H_6 and CH_4, and CO and C_2H_6, respectively. The larger spread of the CO/CH_4 measurements (*y*-axis in Figure 7) is consistent with the correlation found between these species, which is significantly weaker than the correlation between C_2H_6 and CH_4.

The underlying causes of the considerable scatter in Figure 7 might be a byproduct of differences in formative conditions and (possible) post-formative evolution. In particular, nebular models predict wide ranges in abundances of hypervolatile species within the large comet-forming region (Willacy et al. 2015; Drozdovskaya et al. 2016). At the same time, outgassing

patterns that differ among species and with time were observed in 67P by *Rosetta*, with CH_4 showing a diurnal pattern that was distinctly different from the pattern of CO and C_2H_6 (Luspay-Kuti et al. 2015; Bockelée-Morvan et al. 2016; Fink et al. 2016). If similar effects are important among the larger population of comets, they might also contribute to the scatter in abundances derived by snapshot remote-sensing studies, such as those in Figure 7. Separating primordial from evolutionary effects in comets is an extraordinary difficult task, which will benefit from high-cadence campaign studies (see also Dello Russo et al. 2016; DiSanti et al. 2016).

The two in situ measurements of 67P are outliers in both CO/CH_4 and C_2H_6/CH_4. It will be interesting to compare these results from $R_h = 3.15$ au to their corresponding abundance ratios in 67P near perihelion, when the latter become available. Of the comets that were studied by remote sensing, C/2006 W3 (Christensen) has the highest abundance ratio of CO/CH_4. At $R_h < 2$ au, the most similar CO/CH_4 abundance ratios were measured in Hyakutake, C/2013 R1 (Lovejoy), C/2009 P1 (Garradd), Hale-Bopp, and C/1999 S4 (LINEAR), as indicated in Figure 7. This group also had CO/H_2O exceeding ~10% (sometimes referred to as *CO-rich comets*), with the exception of C/1999 S4 LINEAR, which was depleted in all measured volatiles and has a large uncertainty in its CO/CH_4 ratio. Another notable comparator is C/2009 P1 (Garradd), in which the production rate of CO (but not H_2O) increased nearly monotonically from ~2.5 au pre-perihelion to ~2 au post-perihelion (McKay et al. 2015), with a value of ~60% relative to water reported from observations at 2.0 au post-perihelion using the HRI-IR spectrometer on the *Deep Impact* flyby spacecraft (Feaga et al. 2014). A similar trend was not observed in C/2006 W3, at least post-perihelion, where Q(CO) decreased by a factor of ~4 from 3.25 to 4.73 au (Figure 5).

7. Conclusion

CRIRES at ESO-VLT revealed strong infrared emissions in comet C/2006 W3 (Christensen) from the three primary volatiles (CO, CH_4, and C_2H_6) with the lowest equilibrium sublimation temperatures of the species that are commonly studied in comets (24 K, 31 K, and 44 K, respectively; Yamamoto 1985). The absolute production rates of these species at $R_h = 3.25$ au exceeded those measured (for the same volatile) in a number of comets observed at R_h within 1–2 au. Their abundances in C/2006 W3 scaled as $CO/CH_4/C_2H_6 \approx 100/4.4/2$, based on independent measurements on two individual dates (UT OCT. 7 and OCT. 8, 2009) that showed highly consistent results. The observed ratios between the symmetric hydrocarbons (CH_4, C_2H_6) and CO are in agreement with the upper limits reported for comet 29P/Schwassmann-Wachmann 1 at $R_h = 6.26$ au (Paganini et al. 2013). Furthermore, the observed methane-to-ethane ratio falls within the range of previously studied comets at $R_h < 2$ au, while CO/CH_4 is comparatively high and very similar to the in situ measurements at ~10 km from the nucleus of the *Rosetta* target comet 67P/Churyumov-Gerasimenko at $R_h = 3.15$ au (Le Roy et al. 2015).

With its perihelion distance of 3.126 au, comet C/2006 W3 (Christensen) did not enter the zone where water sublimation strongly dominates the gas production during its 2009 apparition. However, its high gas productivity allowed for detections of various primary species at millimeter or submillimeter (Bockelée-Morvan et al. 2010; de Val-Borro et al. 2014) and infrared (Ootsubo et al. 2012, this work) wavelengths. Together, these multiwavelength investigations revealed the most in-depth view possible for the activity and composition of C/2006 W3. The coma was abundant in CO, with reported production rates ranging from ~3 to ~5.5×10^{28} s^{-1} at $R_h = 3.2$–3.3 au (post perihelion), decreasing to ~1×10^{28} at 4.7 au. Other abundant primary volatiles in the coma included CO_2, H_2O, CH_4, CH_3OH, C_2H_6, H_2S, and HCN. The detections of H_2O (*Herschel Space Observatory*) and CO (this work) imply a coma abundance of $H_2O/CO \approx 20\%$ at $R_h \sim 5$ au. This value most likely does not represent their relative abundances in the bulk nucleus.

Our understanding of coma composition and nucleus outgassing is still biased toward heliocentric distances smaller than 2 au. The observations of C/2006 W3 (Christensen) add to the extremely sparse sample of distant comets (previously dominated by Hale-Bopp and 29P/Schwassmann-Wachmann 1, see Section 1 and Womack et al. 2017), in which primary volatiles have been detected. Thus the measurements in C/2006 W3 of both absolute gas production and relative abundances in the coma are of high value for constraining models of (plausibly CO-driven) nucleus sublimation beyond $R_h = 3$ au.

We thank the anonymous referee for comments that substantially improved the paper, and D. Bockelee-Morvan, M. de Val-Borro, H. Kawakita, K. Kossacki, and K. Altwegg for interesting and helpful discussions. Various team members gratefully acknowledge NASA's Planetary Astronomy (09-PAST09-0034; 11-PAST11-0045), Astrobiology (13-13NAI7_2-0032), Solar System Observations (15-SSO15_2-0028; NNX12AG24G), and Planetary Atmospheres (NNX12AG60G) programs, the NSF Planetary Astronomy Grants (AST-1616306, AST-1615441, AST-1211362, and AST-0807939), The German–Israeli Foundation for Scientific Research and Development, International Space Science Institute (Bern, Switzerland) Team 361, and Univ. of Missouri – St. Louis Grants Incentive Funds (for covering the page charges).

Appendix
Fluorescence *g*-factors and Curve of Growth

In fluorescence, a molecule in its ground-vibrational state is "pumped" to a higher mode of vibration by absorbing an infrared solar photon. For fundamental bands, radiative decay back to the ground-vibrational state follows, giving rise to the observed emission. This formalism has been incorporated in modeling fluorescence g-factors [photons s^{-1} $molecule^{-1}$, or in energy units W $molecule^{-1}$] for CH_4 (Gibb et al. 2003), C_2H_6 (Villanueva et al. 2011b), and CO (Paganini et al. 2013), which are all computed assuming optically thin conditions. We used these models to interpret the spectra from comet C/2006 W3.

We also applied newly developed g-factors for CO and CH_4 from G. L. Villanueva et al. (2017, in preparation). Here we describe this formalism in sufficient detail for the present work. The Villanueva et al. g-factors agree with the aforementioned models for optically thin conditions, but also include optical depth (τ) effects (see Sections 4.3–4.4). The latter describe the reduction in intensity of the flux in the solar pump at a given location in the coma. Since the fluorescence efficiency depends strongly on the intensity of the pump, the effective g-factor is reduced compared to the optically thin case.

Quantitatively, the optical depth $\tau = K^{\rm eff} N$, where N is the column density [molecules m^{-2}] and $K_{\rm eff}$ [m^2 $molecule^{-1}$] is the extinction coefficient (effective cross section), after accounting for attenuation in the excitation pumps along the

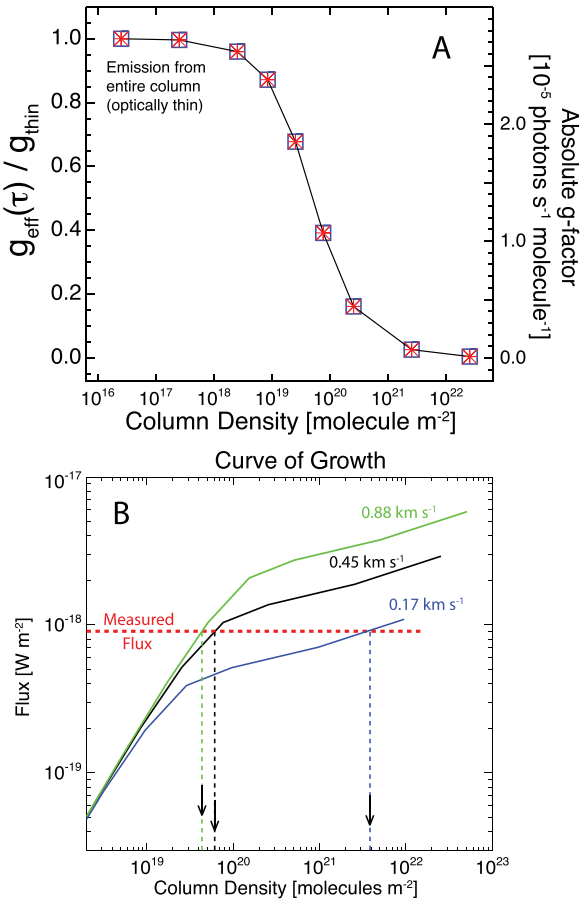

Figure 8. Panel (A): ratio between the g-factors (T_{rot} = 14 K) of the CO P1 line assuming optically thick and optically thin conditions as a function of column density. Panel (B): three curves of growth for the CO P1 line: the modeled flux (y-axis) is calculated from the assumed column density (x-axis) via Equation (2). The measured flux of each detected line is then placed on its corresponding curve of growth to identify the value of the retrieved column density. The three curves of growth assume different gas outflow velocities, as indicated in the figure.

Sun-comet line-of-sight. For comet C/2006 W3, the Sun-comet line was directed nearly away from the observer, since the solar phase angle was $\leqslant 18^{\circ}$ for all observations (Table 1). For emission lines that are not velocity resolved (as is the case for CRIRES), the ratio between the optically thin g-factor ($g_{\rm thin}$) and the effective g-factor in the optically thick regime ($g_{\rm eff}(\tau)$) is shown in Figure 8(A) as a function of column density. In the limit $\tau \gg 1$, $g_{\rm eff}(\tau) \rightarrow g_{\rm thin}/\tau$. At the other extreme, in the limit of $\tau \rightarrow 0$, $g_{\rm eff}(\tau) \rightarrow g_{\rm thin}$, and the emerging flux varies linearly with column density. Like in the optically thin case, the g-factors vary as $R_{\rm h}^{-2}$ and also depend on rotational temperature.

Using $g_{\rm eff}(\tau)$ (W molecule^{-1}), we can retrieve the column density from the measured line flux by modeling the curves of growth for individual emission lines. A representative example with three curves of growth for CO is shown in Figure 8(B). The x-axis covers a wide range of assumed column densities. The y-axis shows the predicted flux at geocentric distance Δ [m] for a field of view (FoV) with a projected area at the comet $A_{\rm FoV}$ [m^2], and telluric transmittance (trn) at the Doppler-shifted line frequency, following the relationship:

$$F = \frac{A_{\rm FoV}}{4\,\pi\,\Delta^2}\; N\; g_{\rm eff}\; \mathrm{trn}. \qquad (2)$$

The measured flux of each detected line is then placed on its corresponding curve of growth to identify the value of the retrieved column density, as marked in Figure 8(B) with downward-pointing arrows. These arrows indicate the values of the column density corresponding to the same measured flux ($\sim 9 \times 10^{-19}$ W m^{-2} for the example shown), parameterized for three different values of the gas expansion velocity ($v_{\rm exp}$; we assume a spherically symmetric outflow).

Note the strong dependence of retrieved column density on $v_{\rm exp}$. At low outflow velocity ($v_{\rm exp} = 170$ m s^{-1}), the measured flux (red dashed line) intersects the strongly nonlinear part in the curve of growth. Increased outflow velocities (shown for $v_{\rm exp} = 450$ m s^{-1}, and 880 m s^{-1}) successively place the measured flux closer to the linear (and therefore optically thin) portion of the curve. This is because molecules ejected from the nucleus at different angles have differing sunward-projected velocities, and this increases the dispersion in pumping frequencies along a given line of sight through the coma (see Greenstein 1958 and Appendix of DiSanti et al. 2001). Conversely, smaller projected velocity dispersions (related to small $v_{\rm exp}$) lead to molecules in the coma absorbing solar photons at (nearly) the same frequency, and thereby to increased shadowing by foreground (i.e., sunward) molecules, resulting in stronger effective line opacities.

We assumed that the outflow velocity follows the relationship $v_{\rm exp} = 800\ R_{\rm h}^{-0.5}$. Importantly, this assumption leads to $v_{\rm exp} \approx 440$ m s^{-1} at $R_{\rm h} = 3.25$ au ($v_{\rm exp} \approx 370$ m s^{-1} at $R_{\rm h} =$ 4.7 au), in excellent agreement with measurements of velocity-resolved rotational lines in C/2006 W3 (Bockelée-Morvan et al. 2010; de Val-Borro et al. 2014). This agreement validates our assumed $v_{\rm exp}$ and mitigates an otherwise large systematic uncertainty in the column density (and hence production rate, including for optically thin emission).

We assume that the opacity in the CO lines is strongly dominated by attenuation in the solar pump. We verified that after accounting for optical depth in the pump, we obtain line-by-line production rates that agree within their uncertainties, even for lines of sight near the nucleus. Optical depth might also reduce the emitted quanta that reach the observer for some conditions. This effect is mitigated by the Q-curve formalism, as detailed in Section 4.4. The uncommonly large growth factor (i.e., the ratio of terminal to nucleus-centered production rate) in Figure 4(A) accounts for contributions from slit losses, extinction in the pump, and (if important) extinction in the emission. More complex radiative transfer treatments such as 3D Monte Carlo simulations (e.g., Fougere et al. 2013, 2012) are outside the scope of this paper. A more rigorous treatment requires including additional parameters that cannot be easily constrained. Our simplified approach is sufficient to identify emissions from lines of sight that are significantly affected by optical depth and to circumvent them in obtaining our finalized production rates.

References

A'Hearn, M. F., Belton, M. J. S., Delamere, W. A., et al. 2011, Sci, 332, 1396
Biver, N., Bockelée-Morvan, D., Colom, P., et al. 2002, EM&P, 90, 5
Biver, N., Rauer, H., Despois, D., et al. 1996, Natur, 380, 137
Bockelée-Morvan, D., Crovisier, J., Erard, S., et al. 2016, MNRAS, 462, S170
Bockelée-Morvan, D., Hartogh, P., Crovisier, J., et al. 2010, A&A, 518, L149
Boehnhardt, H., Mumma, M. J., Villanueva, G. L., et al. 2008, ApJL, 683, L71
Bonev, B. P. 2005, PhD thesis, Univ. Toledo http://astrobiology.gsfc.nasa.gov/Bonev_thesis.pdf
Bonev, B. P., Mumma, M. J., DiSanti, M. A., et al. 2006, ApJ, 653, 774

Bonev, B. P., Villanueva, G. L., Paganini, L., et al. 2013, Icar, 222, 740
Brooke, T. Y., Weaver, H. A., Chin, G., et al. 2003, Icar, 166, 167
Christensen, E. J., Buzzi, L., Luppi, F., et al. 2006, IAUC, 8777, 1
Clough, S. A., Shephard, M. W., Mlawer, E. J., et al. 2005, JQSRT, 91, 233
Cochran, A., Barker, E. S., & Cochran, W. 1980, AJ, 85, 474
Cochran, A. L., & Cochran, W. D. 1991, Icar, 90, 172
Cochran, A. L., Cochran, W. D., Barker, E. S., & Storrs, A. D. 1991, Icar, 92, 179
Crovisier, J. 1999, Natur, 399, 640
Crovisier, J., Biver, N., Bockelée-Morvan, D., et al. 1995, Icar, 115, 213
Dello Russo, N., DiSanti, M. A., Mumma, M. J., Magee-Sauer, K., & Rettig, T. W. 1998, Icar, 135, 377
Dello Russo, N., Kawakita, H., Vervack, R. J., & Weaver, H. A. 2016, Icar, 278, 301
Dello Russo, N., Mumma, M. J., DiSanti, M. A., Magee-Sauer, K., & Novak, R. 2001, Icar, 153, 162
Dello Russo, N., Vervack, R. J., Weaver, H. A., et al. 2009, ApJ, 703, 187
de Val-Borro, M., Bockelée-Morvan, D., Jehin, E., et al. 2014, A&A, 564, A124
DiSanti, M., Bonev, B. P., Dello Russo, N., et al. 2017, CBET, 4357, 1
DiSanti, M. A., Bonev, B. P., Gibb, E. L., et al. 2016, ApJ, 820, 34
DiSanti, M. A., Bonev, B. P., Magee-Sauer, K., et al. 2006, ApJ, 650, 470
DiSanti, M. A., & Mumma, M. J. 2008, SSRv, 138, 127
DiSanti, M. A., Mumma, M. J., Dello Russo, N., et al. 1999, Natur, 399, 662
DiSanti, M. A., Mumma, M. J., Dello Russo, N., & Magee-Sauer, K. 2001, Icar, 153, 361
DiSanti, M. A., Villanueva, G. L., Paganini, L., et al. 2014, Icar, 228, 167
Drozdovskaya, M. N., Walsh, C., & van Dishoeck, E. F. 2016, MNRAS, 462, 977
Feaga, L. M., A'Hearn, M. F., Farnham, T. L., et al. 2014, AJ, 147, 24
Festou, M. C., Gunnarsson, M., Rickman, H., et al. 2001, Icar, 150, 140
Fink, U., Doose, L., Rinaldi, G., et al. 2016, Icar, 277, 78
Fougere, N., Combi, M. R., Rubin, M., & Tenishev, V. 2013, Icar, 225, 688
Fougere, N., Combi, M. R., Tenishev, V., et al. 2012, Icar, 221, 174
Gibb, E. L., Mumma, M. J., Dello Russo, N., DiSanti, M. A., & Magee-Sauer, K. 2003, Icar, 165, 391
Greenstein, J. L. 1958, ApJ, 128, 106
Gunnarsson, M., Bockelée-Morvan, D., Biver, N., Crovisier, J., & Rickman, H. 2008, A&A, 484, 537
Gunnarsson, M., Rickman, H., Festou, M. C., Winnberg, A., & Tancredi, G. 2002, Icar, 157, 309
Hoban, S., Mumma, M., Reuter, D. C., et al. 1991, Icar, 93, 122
Jewitt, D., Senay, M., & Matthews, H. 1996, Sci, 271, 1110
Käufl, H., Ballester, P., Biereichel, P., et al. 2004, Proc. SPIE, 5493, 1218
Kawakita, H., Dello Russo, N., Vervack, R., et al. 2014, ApJ, 788, 110
Knight, M. M., & Schleicher, D. G. 2015, AJ, 149, 19
Korsun, P. P., Ivanova, O. V., & Afanasiev, V. L. 2008, Icar, 198, 465
Korsun, P. P., Kulyk, I., Ivanova, O. V., et al. 2016, A&A, 596, A48
Kossacki, K. J., & Szutowicz, S. 2015, Icar, 250, 595
Lamy, P. L., Imre, T., & Weaver, H. A. 2014, ApJL, 794, L9
le Roy, L., Altwegg, K., Balsiger, H., et al. 2015, A&A, 583, A1
Lippi 2010, PhD thesis, Technische Universität Braunschweig, Germany (UNI-Ed.)
Lippi, M., Villanueva, G. L., DiSanti, M. A., et al. 2013, A&A, 551, A51
Luspay-Kuti, A., Hässig, M., Fuselier, S. A., et al. 2015, A&A, 583, A4
Magee-Sauer, K., Mumma, M. J., DiSanti, M. A., Dello Russo, N., & Rettig, T. W. 1999, Icar, 142, 498
Marsden, B. G., & Roemer, E. 1982, in Comets, ed. L. L. Wilkening (Tucson, AZ: Univ. Arizona Press), 707
Mazzotta Epifani, E., Palumbo, P., Capria, M. T., et al. 2007, MNRAS, 381, 713
Mazzotta Epifani, E., Palumbo, P., Capria, M. T., et al. 2008, MNRAS, 390, 265
Mazzotta Epifani, E., Palumbo, P., Capria, M. T., et al. 2009, A&A, 502, 355
McKay, A. J., Chanover, N. J., Morgenthaler, J. P., et al. 2012, Icar, 220, 277
McKay, A. J., Cochran, A. L., DiSanti, M. A., et al. 2015, Icar, 250, 504
Meech, K. J., Pittichová, J., Bar-Nun, A., et al. 2009, Icar, 201, 719
Meech, K. J., & Svoren, J. 2004, in Comets II, ed. M. C. Festou, H. U. Keller, & H. A. Weaver (Tucson, AZ: Univ. Arizona Press), 317
Meech, K. J., Yang, B., Kleyna, J., et al. 2013, ApJL, 776, L20
Mumma, M. J., Bonev, B. P., Villanueva, G. L., et al. 2011, ApJL, 734, L7
Mumma, M. J., & Charnley, S. B. 2011, ARA&A, 49, 471
Mumma, M. J., DiSanti, M. A., Dello Russo, N., et al. 2003, AdSpR, 31, 2563
Nakano, S. 2011, Oriental Astronomical Association, Computing Section Circular, Nakano Note NK 2064, http://www.oaa.gr.jp/~oaacs/nk/nk2064.htm
Ootsubo, T., Kawakita, H., Hamada, S., et al. 2012, ApJ, 752, 15
Paganini, L., Mumma, M. J., Boehnhardt, H., et al. 2013, ApJ, 766, 100
Paganini, L., Mumma, M. J., Villanueva, G. L., et al. 2012, ApJL, 748, L13
Paganini, L., Mumma, M. J., Villanueva, G. L., et al. 2014, ApJ, 791, 122
Protopapa, S., Sunshine, J. M., Feaga, L. M., et al. 2014, Icar, 238, 191
Rauer, H., Helbert, J., Arpigny, C., et al. 2003, A&A, 397, 1109
Reach, W. T., Kelley, M. S., & Vaubaillon, J. 2013, Icar, 226, 777
Senay, M. C., & Jewitt, D. 1994, Natur, 371, 229
Villanueva, G. L., Mumma, M. J., Bonev, B. P., et al. 2009, ApJL, 690, L5
Villanueva, G. L., Mumma, M. J., Bonev, B. P., et al. 2012, JQSRT, 113, 202
Villanueva, G. L., Mumma, M. J., DiSanti, M. A., et al. 2011a, Icar, 216, 227
Villanueva, G. L., Mumma, M. J., & Magee-Sauer, K. 2011b, JGR, 116, E08012
Villanueva, G. L., Mumma, M. J., Novak, R. E., & Hewagama, T. 2008, Icar, 195, 34
Willacy, K., Alexander, C., Ali-Dib, M., et al. 2015, SSRv, 197, 151
Womack, M., Sarid, G., & Wierzchos, K. 2017, PASP, 129, 031001
Xie, X., & Mumma, M. J. 1996, ApJ, 464, 457
Yamamoto, T. 1982, A&A, 109, 326
Yamamoto, T. 1985, A&A, 142, 31